Supporting information

Self-powered InAs nanowire detector arrays for extended-SWIR spectrometry at room temperature

Yang Yu[a], Wei Wen Wong[a], Zhe Li[a], Dawei Liu[a], Jinyuan Chen[b], Seyed Saleh Mousavi Khaleghi[b], Yue Bian[a], Kosala Dhanawansha[a], Li Li[a], Hongwei Liu[c], Xiaoxue Xu[d], Monica Allen[e], Jeffery Allen[e], Hark Hoe Tan[a], Chennupati Jagadish[a], Kenneth Crozier[b], Ziyuan Li[a,*], Chaohao Chen[d,f*], and Lan Fu[a,*]

[a] *Australian Research Council Centre of Excellence for Transformative Meta-Optical Systems, Department of Electronic Materials Engineering, Research School of Physics, The Australian National University, Canberra, ACT 2600, Australia*

[b] *Australian Research Council (ARC) Centre of Excellence for Transformative Meta-Optical Systems (TMOS), University of Melbourne, Victoria, Australia*

[c] *The Australian Centre for Microscopy and Microanalysis, The University of Sydney, Sydney, New South Wales, 2006, Australia*

[d] *School of Biomedical Engineering, Faculty of Engineering and Information Technology, University of Technology Sydney, NSW 2007, Australia*

[e] *Air Force Research Laboratory, Munitions Directorate, Eglin AFB, FL 32542, USA*

[f] *Australian Research Council Centre of Excellence for Transformative Meta-Optical Systems, The University of Technology Sydney, Ultimo, NSW 2007, Australia*

Corresponding emails: ziyuan.li@anu.edu.au, chaohao.chen@uts.edu.au, lan.fu@anu.edu.au

1. MOCVD Growth process and results

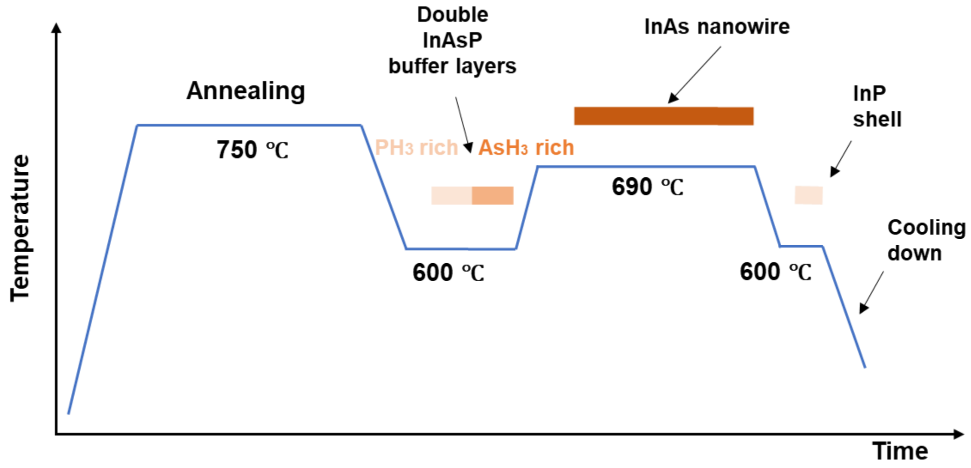

Figure S1: Schematic illustrating the InAs/InP core-shell nanowire array growth sequence.

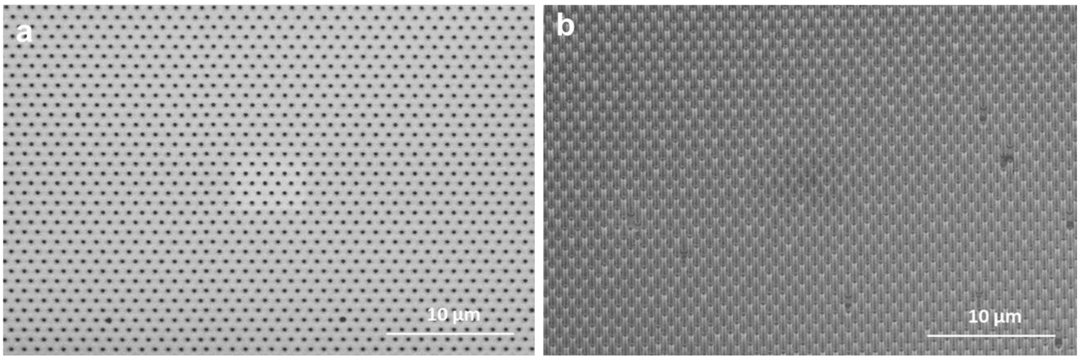

Figure S2: Large-area scanning electron microscopy (SEM) images (top view) of InAsP buffer layers (a) and InAs nanowires (b) grown from mask openings with 530 nm diameter.

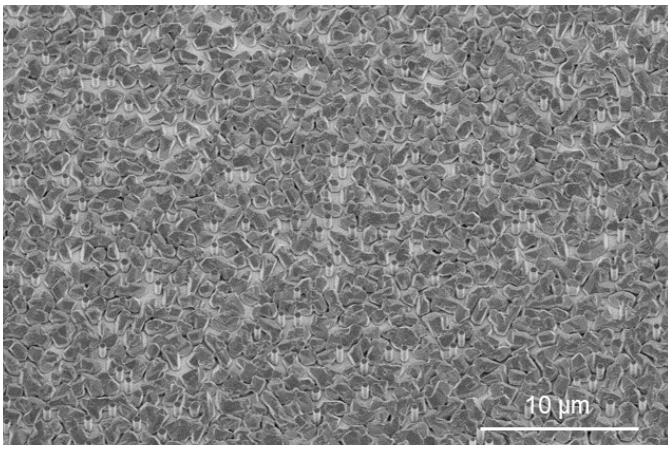

Figure S3: InAs nanowires grown from circular mask openings with a diameter of 400 nm on an InP substrate without any buffer layer.

2. Device characterisation

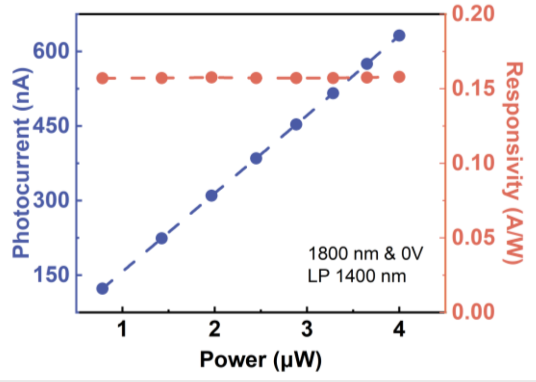

Figure S4: Photocurrent and responsivity characteristics of S-4 device measured under an 1800 nm illumination (1400 nm long-pass filter applied) and zero bias with incident illumination power ranging from 0.78 μW to 4.05 μW.

Power-dependent photocurrent and responsivity measurements were conducted at room temperature without bias, under illumination at a wavelength of 1800 nm. A long-pass filter with a cut-on wavelength of 1400 nm was used. As the illumination power increases from 0.78 μW to 4.05 μW, the photocurrents show a linear increase while the responsivities remain constant, ensuring stable performance across varying light conditions.

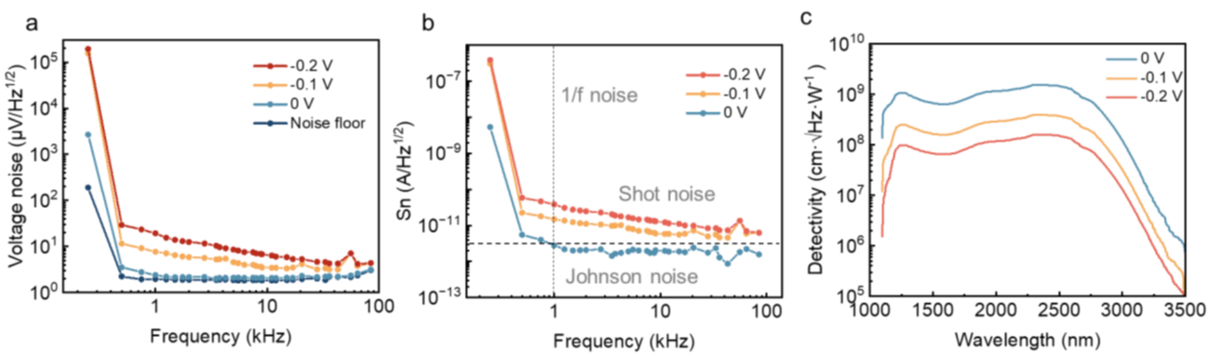

Figure S5: (a) Frequency-dependent voltage noises from 250 Hz to 85 kHz, (b) current noise spectral density, and (c) bias-dependent detectivity spectra measured for device S-4 at the room temperature.

For a single-element infrared photodetector, current-noise density (*Sn*) at a specific frequency is usually used in detectivity calculation. We first measured the voltage noise (S_v) spectra from 250 Hz to 85 kHz (**Figure S5a**). The bias voltage was set to 0 V. At 1 kHz, the S_v is 2.4×10^{-6} V·Hz$^{-1/2}$, and noise floor (S_f) is 1.954×10^{-6} V·Hz$^{-1/2}$. Therefore, the current noise spectral density *Sn* was obtained by quadrature subtraction and conversion through the transimpedance gain *G* of 5×10^5 V A^{-1} from the pre-amplifier:

$$S_n = \frac{\sqrt{{S_v}^2 - {S_f}^2}}{\mathrm{G}}, (1)$$

So, the *Sn* can be calculated to be 2.78 × 10^{-12} A·$Hz^{-1/2}$ at 1 kHz as shown in **Fig. S5b**.

We then calculated the noise equivalent power (*NEP*), another crucial figure of merit for assessing photodetector sensitivity. *NEP* is defined as the ratio of the measured *Sn* to the corresponding responsivity (*NEP = Sn/R*). From **Fig. 3e** in the main text, the device peak responsivity is 0.215 A/W at 2300 nm. In general, a lower *NEP* indicates a stronger capability to distinguish between the desired signal and unwanted noise. Here, the optimal *NEP* values are calculated to be 1.29 × 10^{-11} W·$Hz^{-1/2}$ at 2300 nm at the room temperature, indicating the exceptional sensitivity of our InAs nanowire array photodetector to detect extremely low power levels at the extended-SWIR wavelength.

The detectivity measures the device's ability to responds to weak incident signals. In this work, we obtained the measured specific detectivity (D_M*) from:

$$D_M{}^* = \frac{\sqrt{A}}{S_n}\mathrm{R} = \frac{\sqrt{A}}{NEP}, (2)$$

where *A* represents active area of the device, with a value of 4×10^{-4} cm^2. Therefore, the room temperature D_M* is as high as 1.6 × 10^9 cm·$Hz^{1/2}$·W^{-1} in the short-wave infrared (SWIR) region without any external bias (**Fig. S5c**), comparable to that reported in state-of-the-art commercial photodetectors (approximately 3 × 10^9 cm·$Hz^{1/2}$·W^{-1}).[1]

For SWIR photodetectors, many existing reports directly use dark current to calculate the detectivity[2], as the main noise sources are shot noise (due to the dark current I_d) and Johnson noise (due to the random motion of carriers with average thermal energy *kT*)[3]. Therefore, the *Sn* can be estimated using the shot noise ($2qI_d$) and Johnson noise ($4kT/R_d$):

$$S_n = \sqrt{2qI_d + \frac{4kT}{R_d}}, (3)$$

Then, the calculated detectivity (D_C*) can be defined as:

$$D_c{}^* = \sqrt{\frac{A}{2qI_d + \frac{4kT}{R_d}}}\mathrm{R}, (4)$$

where *R* is corresponding responsivity, *A* is active area of the array device, *k* is Boltzmann constant, *T* is temperature, and I_d is the dark current, which was chosen to be 4.37 μA at -0.02 V. R_d is the dynamic resistance, which can be defined as $R_d = (dI_d/dV|_{V=0})^{-1}$. Therefore, the calculated peak D_C* including shot noise and Johnson noise, is 2 × 10^9 cm·$Hz^{1/2}$·W^{-1}, which agrees well with the measured D_M* described above.

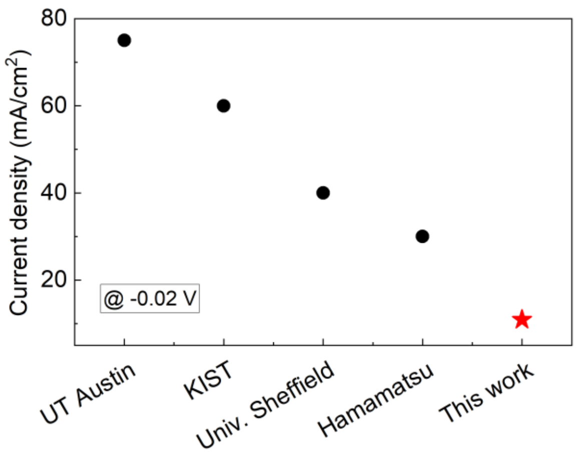

Figure S6: Comparison of room-temperature dark current density at a reverse bias of -0.02 V (~ zero bias) between the nanowire photodetector and various types of reported InAs photodetectors, including InAs photovoltaic detectors (Hamamatsu);[1] InAs APDs (UT Austin);[4] InAs thin film (KIST, Korea);[5] InAs photodiode (Univ. Sheffield).[6]

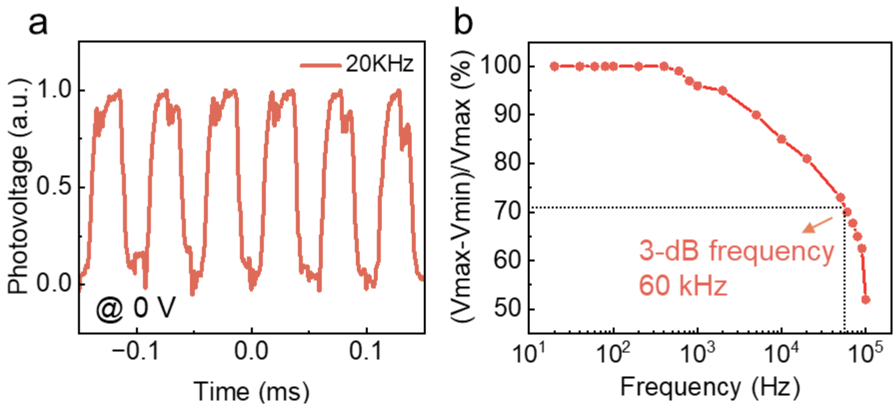

Figure S7: (a) Temporal response of the photovoltage under a pulsed laser illumination (1550 nm) at 20 kHz without bias. (b) Differential voltage (dB) versus frequency, showing the 3-dB cut-off frequency of ~ 60 kHz.

3. Single-pixel imaging using an InAs nanowire array photodetector

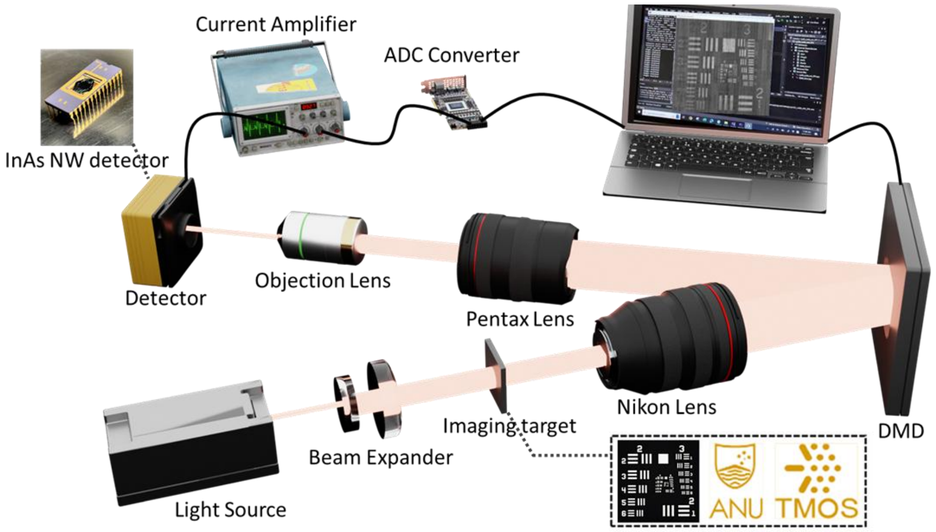

Figure S8: Schematic of a single-pixel imaging setup.

We demonstrate the broadband imaging capability of the InAs nanowire-array photodetector by integrating the fabricated device into a DMD-based single-pixel imaging system, where it serves as the photosensitive element (**Figure S8**). In this computational imaging approach, a sequence of spatially encoded patterns is projected onto the object using the DMD, and the transmitted or reflected intensity associated with each pattern is recorded by a single detector.[7] Compared with conventional raster-scanning approaches, DMD-based spatial encoding removes mechanical scanning and provides a more efficient route to image acquisition, while allowing the spatial resolution to be defined by the projected pattern set.[2] As in other single-pixel imaging systems, however, higher spatial resolution requires a larger number of projected patterns and therefore a longer acquisition time. This strategy enables e-SWIR imaging with substantially lower cost and system complexity than commercially available e-SWIR camera systems.

In our experiment, an InAs nanowire detector (with diameter of 500 nm and pitch size of 1200nm) was mounted on a standard 28-pin chip carrier and operated at room temperature without external bias. Three imaging targets were used to evaluate the imaging performance: a one-inch 1951 USAF resolution target (Edmund Optics) and two custom reflective targets patterned with the Australian National University (ANU) logo and the ARC Centre of Excellence for Transformative Meta-Optical Systems (TMOS) logo. The custom targets were fabricated by electron-beam lithography followed by lift-off of 10 nm Ti/100 nm Au, providing sufficient reflectivity under SWIR illumination.

4. FDTD simulation on nanowire array geometry dependent absorption for construction of a multipixel response matrix

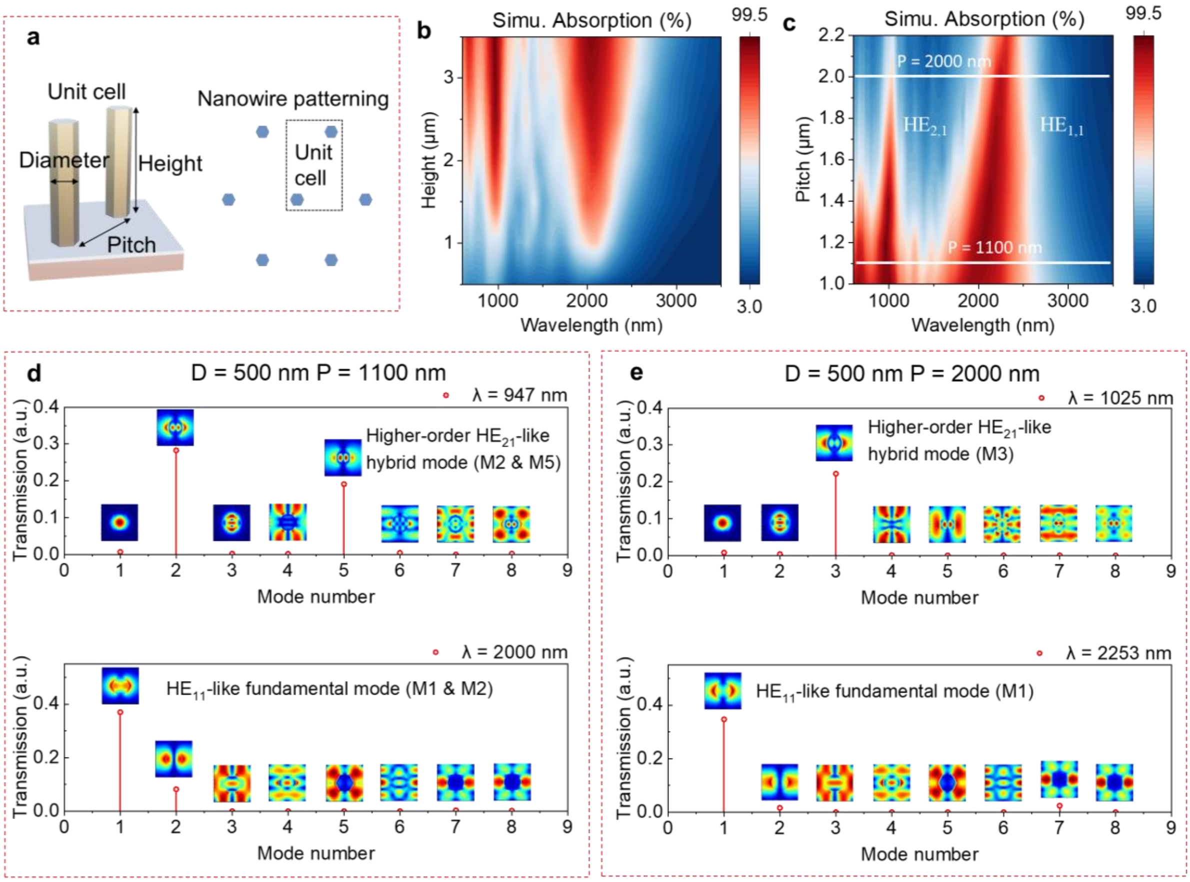

Figure S9: **Optical design and modal analysis of the InAs nanowire arrays. a**, Schematic of the simulated nanowire unit cell and hexagonal array geometry. **b**, Simulated absorption spectra obtained by varying the nanowire height at a fixed diameter of 500 nm and a fixed array pitch of 1100 nm. **c**, Simulated absorption map obtained by varying the array pitch while fixing the nanowire diameter and height at 500 nm and 3500 nm, respectively. Representative pitch values of 1100 and 2000 nm were selected for modal analysis. **d, e**, Modal transmission coefficients and corresponding normalized electric-field distributions at the two principal absorption bands for arrays with pitches of 1100 nm (**d**) and 2000 nm (**e**). The short-wavelength resonances are predominantly associated with an HE_{21}-like higher-order hybrid mode, whereas the long-wavelength resonances are dominated by the fundamental HE_{11}-like mode.

The nanowire geometry was optimized through a sequential series of FDTD simulations. The nanowire diameter was fixed at 500 nm, and the height was first varied at a fixed array pitch. As shown in **Figure S9b**, reducing the nanowire height progressively decreases the absorption because of the reduced optical interaction volume and propagation length within the InAs absorber. A height of 3500 nm was therefore selected to maintain strong absorption while remaining compatible with uniform nanowire growth. The array pitch was subsequently varied while fixing the diameter and height at 500 nm and 3500 nm, respectively (**Fig. S9c**). Increasing the pitch from 1100 to 2000 nm produces more spectrally isolated resonances with narrower linewidths, whereas the more closely packed array exhibits broader and more continuous absorption.

Mode-expansion analysis was performed at the two principal absorption bands for the representative pitches of 1100 and 2000 nm (**Fig. S9d, e**). For the 1100 nm-pitch array, the short-wavelength resonance at 947 nm is dominated by a higher-order hybrid mode (M2), with an additional contribution from M5; whereas the resonance near 2000 nm is primarily supported by the fundamental-like M1 mode. For the 2000 nm-pitch array, the corresponding resonances near 1028 and 2253 nm are predominantly supported by M3 and M1, respectively. Similar field symmetries indicate that M2/M3 belong to the same HE_{21}-like higher-order modal family, whereas M1 is assigned to an HE_{11}-like fundamental mode. The reduced modal overlap at the larger pitch is consistent with weaker inter-nanowire coupling and accounts for its narrower absorption bands.

5. SEM, IV and spectral responsivity measured from the multipixel nanowire spectrometer chip

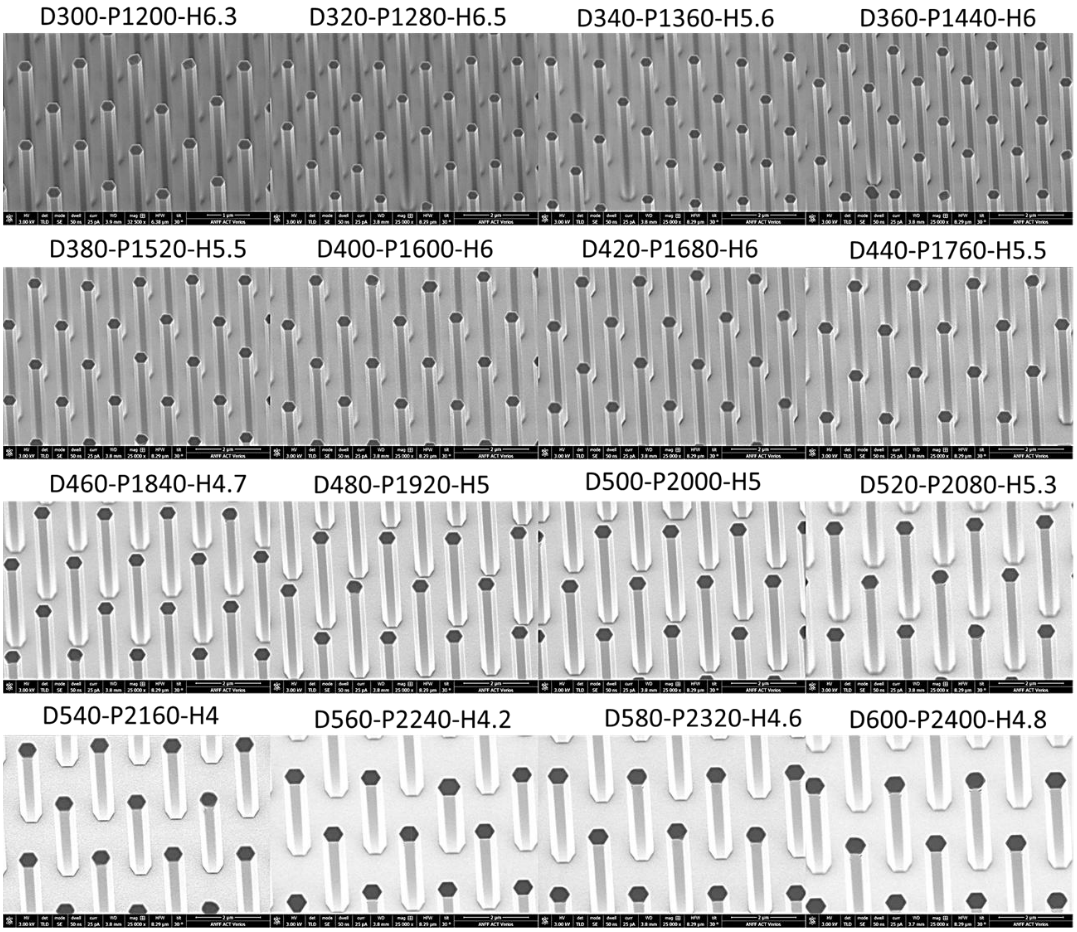

Figure S10: SEM images measured from 16 InAs nanowire arrays grown on the same substrate with increasing diameter and pitch size from D300 nm/P1200 nm to D600 nm/P2400 nm for spectrometer chip fabrication. (D denotes diameter, P denotes pitch size, and H denotes height of the nanowire arrays)

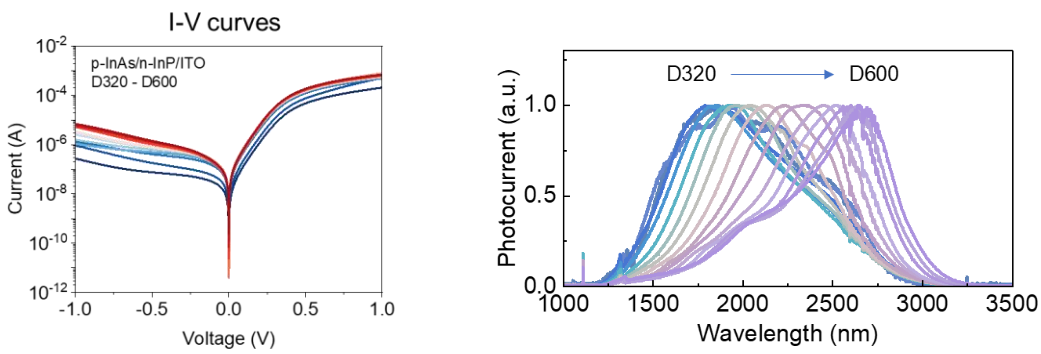

Figure S11: Dark *I-V* curves and photocurrent spectra measured from 15 array pixels with nanowire diameter from 320 nm to 600 nm of the spectrometer. The pixel with diameter of 300 nm (D300) is excluded due to device failure.

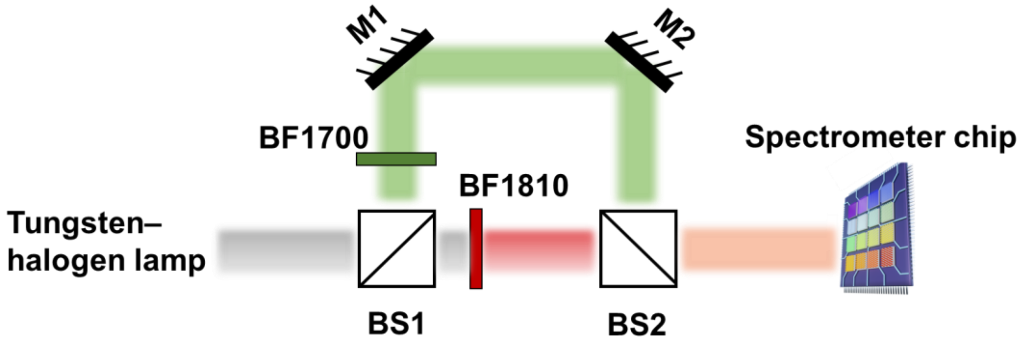

Figure S12: Schematic diagram illustrating the experimental setup for dual peak spectral reconstruction using a tungsten halogen lamp. Bandpass filters (BF) of 1700 nm and 1810 nm were used.

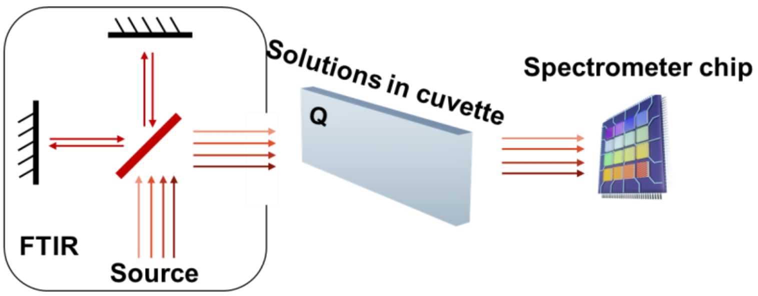

Figure S13: Schematic diagram illustrating the experimental setup for water transmission spectral reconstruction using a Bruker VERTEX 80v FTIR system.

6. Details for hyperspectral imaging

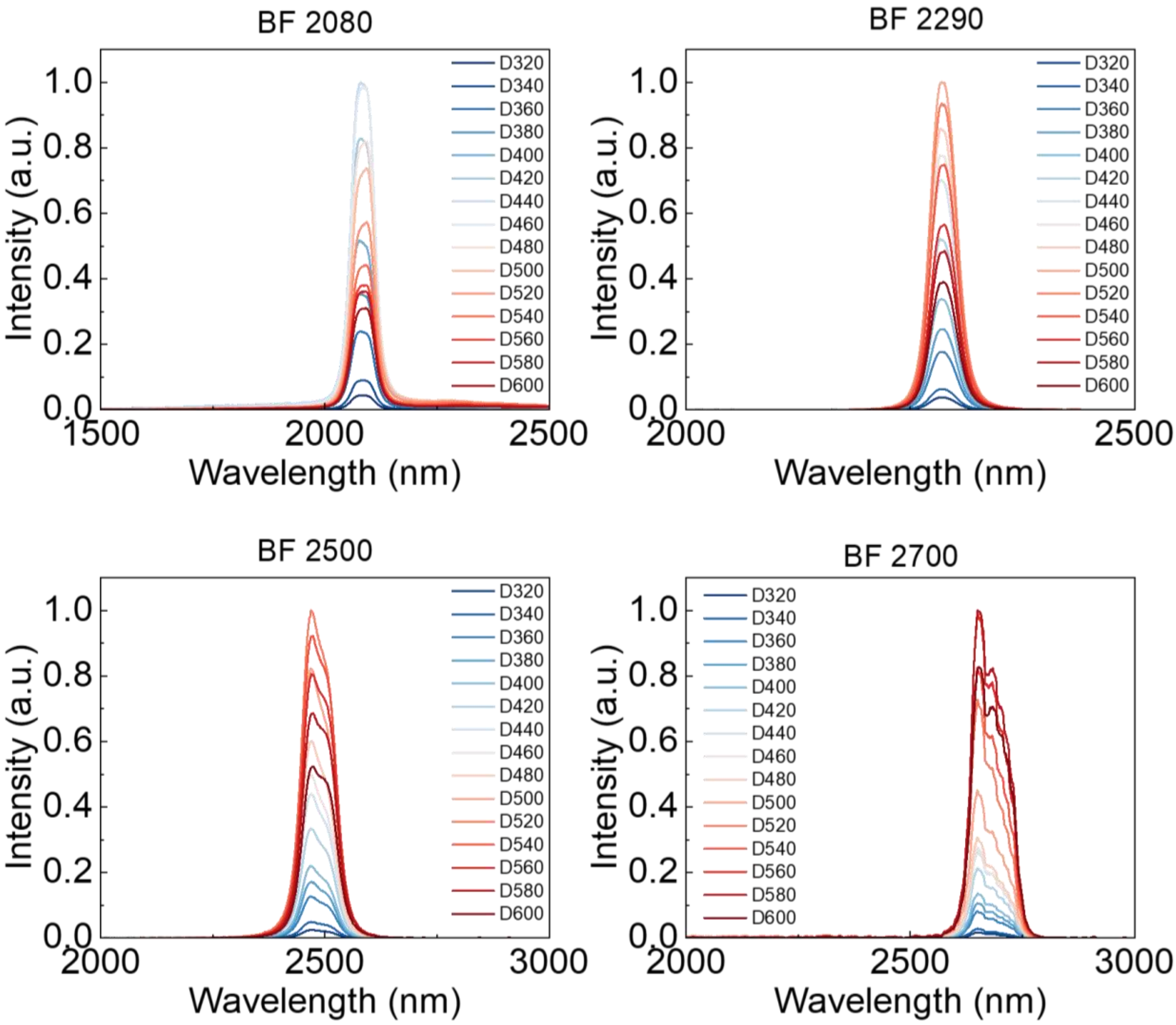

Figure S14: Representative wavelength-resolved photocurrent spectra measured from the 15 detector channels of the InAs nanowire spectrometer chip under four bandpass-filtered (BF) inputs centred at 2080, 2290, 2500, 2700 nm. The integrated photocurrent of each channel was obtained from the area under the corresponding spectral curve.

During the measurement, the mask was mechanically scanned while the spectrometer chip remained fixed, such that light transmitted through each mask pixel was sequentially delivered to the detector area. To improve the accuracy of photocurrent extraction for each detector channel, wavelength-resolved photocurrent spectra were first recorded from the 15 detector channels using the FTIR readout at each spatial position. Each spectrum was then integrated over wavelength to obtain a scalar photocurrent value, yielding a 15-element photocurrent vector for that spatial pixel. Repeating this process over the 10 × 10 mask positions produced a 15 × 100 photocurrent data cube, which was used as the input for pixel-wise spectral reconstruction. Representative wavelength-resolved photocurrent spectra measured under four bandpass-filtered inputs are shown in **Figure S14**.

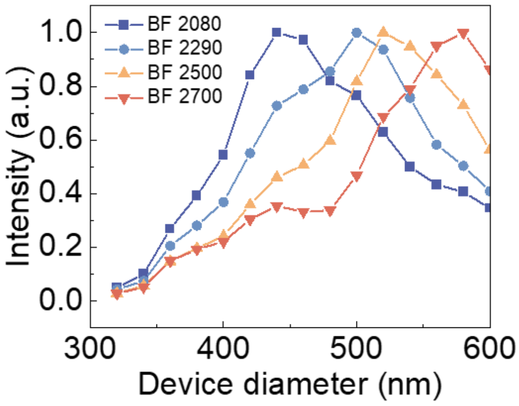

Figure S15: Integrated photocurrent vectors extracted from the wavelength-resolved spectra in **Fig. S14** for four representative bandpass-filtered inputs. Each curve contains the integrated photocurrent values from the 15 detector channels under one bandpass-filtered illumination condition. The different bandpass filters generate distinct photocurrent patterns across the detector library, confirming that the InAs nanowire array provides spectrally diverse measurement channels for reconstructing the spectrum at each spatial pixel.

At each bandpass-filtered input, the photocurrent assigned to detector channel i was obtained by integrating the wavelength-resolved photocurrent spectrum over the measured wavelength range:

$$I_i = \int_{\lambda_{min}}^{\lambda_{max}} i_i(\lambda) d\lambda, \quad (5)$$

where $i_i(\lambda)$ is the measured wavelength-resolved photocurrent spectrum of detector channel i.

The 15 integrated photocurrent values obtained for each incident spectrum were assembled into a photocurrent vector and used as the input for spectral reconstruction, as shown in **Figure S15**.

7. Performance comparison with reported e-SWIR photodetectors and computational spectrometers

Table S1. Performance summary of recently reported e-SWIR detectors (tested at room temperature unless labeled)

	Structure SWIR detector	Operation wavelength (nm)	Spectral tunability	Bias (V)	R (A/W)	D* ($cm \cdot Hz^{-1/2} \cdot W^{-1}$)	Rise/fall time (μs)	Ref
2D material	Quasi-2D Te	2300	No	1	$\sim 2.6 \times 10^2$	$\sim 2 \times 10^9$	48.7/62.7	8
	BP/MoS_2	3600	No	0	N/A	2.34×10^9	56/79	9
	BP/MoS_2	3500	No	0	0.9	1.1×10^{10}	3.7/4	10
	$PdSe_2$ /$MoTe_2$	1700	No	0	~0.01	N/A	337/267	11
	PdSe2/2H−$MoTe_2$	2200	No		~0.04	$\sim 6 \times 10^7$	45/71.5	12
Colloidal quantum dot (CQD)	SWIR HgTe CQD with planar p-n junction	2430	No	0	~0.4	3×10^{10}	184/212	13
InAs-based III-V material	InAs commercial photovoltaic detector	2300	No	-0.5	~0.7	3×10^9	0.7	1
	InAs nanowire array on InAs substrate	1600	No	0	0.44 @150 K	1.25×10^{10} @150 K	25/24	14
	InAsP planar	2400	No	-1	N/A	1×10^9	N/A	15
	InAs nanowire array on InP substrate	2000	No	0.5	0.0014	2.5×10^7	N/A	16
	InAs/InP nanowire array (D530 nm device)	2300	Yes	0	0.215	1.6×10^9 @300 K	7/5	This work
					0.38 @150 K	1.81×10^{11} @150 K		

Table S1 summarizes the performance comparison for the recently reported e-SWIR photodetectors based on different material platforms. Considering all the key device parameters including spectral range/tunability, responsivity, detectivity and speed, our InAs/InP/ITO radial heterojunction nanowire array photodetectors have shown the best overall performance.

Table S2. Summary of recent literatures on computational spectrometer

Category	Year	Reference	Gate-field or bipolar or unipolar	Device structure	Spectral range (μm)	Bias range (V)	R (A/W)	D* ($cm\cdot Hz^{-1/2}\cdot W^{-1}$)	Array size	Spectral resolution
2D material	**2021**	**Nat. Photonics[17]**	**Gate-field**	**Single dualgated photodetector; hBN/BP(13nm) / hBN heterostructure with graphene top gate**	**2-9**	**0.1~0.83 V/nm**	**-**	**-**	**Single pixel**	**90 nm single-peak resolving capability**
	2022	**Nano Lett.[18]**	**Gate-field**	**BP/MoS_2 heterojunction diode on SiO_2/Si substrate**	**1.7-3.6**	**-20~20**	**-**	**7×10^7 Jones@ zero source-drain bias**	**Single pixel**	**43 nm (1.7~3.6μ m) 20 nm(2.8~3.6) single-peak resolving capability**
	2022	Nat. Commun.[19]	Gate-field	Single back-gated photodetector based on a ReS_2/Au/WSe_2 van der Waals heterostructure	1.15~1.47	-17~29	~0.001	-	Single pixel	20 nm
	2022	Science[20]	Gate-field	Single van der Waals junction photodetector: MoS_2/WSe_2 heterojunction encapsulated in h-BN, with a graphene bottom gate	0.405~0.845	-10~10	-	-	Single pixel	3 nm
Colloidal quantum dot (CQD) photodiodes	2026	Nat. Photonics[21]	Unipolar	Stacked large-bandgap PbS CQDs/p-doped PbS CQDs/small-bandgap PbS CQDs	0.4~1.7	0-0.75	-	Above 10^{10} Jones within 400~1700 nm @0V; Above 10^{12} Jones within 400~1700 nm @0.68V; Above 4.32×10^{10} Jones within 0~0.75V; 1.31×10^{13}	1280×1024	1 nm

								Jones @0.68V		
Stacked organic photodiodes	2024	Nat. Electron.[22]	Bipolar	Back-to-back Schottky diode design and an organic ternary bulk heterojunction: PEIE/PNDIT-F3N/PTB7-Th:P3HT:PC71BM	0.4-0.76	-15~15		~10^{11} Jones; not given@ 0 V	8×8	~5 nm
	2025	Adv. Materials[23]	Bipolar	Asymmetric back-to-back organic photodiode: Ag/MoO_3/BHJ_2/ZnO/BHJ_1/PEDOT:PSS/ITO	0.3~1	-0.6~0.6	0.028	-	Single pixel	1 nm
Si	2020	Nano Lett.[24]	Bipolar	Vertically stacked dual PIN junctions; top detector is a vertical silicon nanowire array (doped p+/i(n-)/n+), bottom is a planar mesa detector (doped n+/i(n-)/p+).	0.4~0.8	-3~3		-	24	6 nm
	2019	**ACS Photonics[25]**	**Unipolar**	**Al grating/heavily p-doped Si: tunable response by varying the grating pitch, with photodetection based on free-carrier absorption in Si.**	**2.2~3.8**	**0.0015**	**0.00017**	**-**	**20**	**40 nm single-peak resolving capability**
III-V material	2025	Nat. Photonics[26]	Bipolar	Vertically cascaded n-p-n photodiode: n-GaN/i-GaN/p-GaN/Graded i-AlGaN/n-AlGaN on	0.25~0.365	-10~6	~0.5	-	10×10	1 nm

				Sapphire substrate						
	2024	Nat. Commun.[27]	Bipolar	Single vertically stacked p-graded-n junction: p+ GaAs contact/p-AlGaAs/ InGaP hole barrier/ compositionally graded n-AlGaAs/n+ GaAs contact	0.48~0.82	-10~0	0.51	1.86×10^{13} @-10 V	Single pixel	10 nm
	2026	**This work**	**Unipolar**	**InAs/InP p-n core-shell nanowire array**	**1~3**	**0**	**0.215** **0.38 @150 K**	**1.6×10^{9}** **1.81×10^{11} @150 K**	**16**	**17 nm single-peak resolving capability** **93 nm dual-peak resolving capability**

Table S2 summarizes the performance comparison for the recently reported computational spectrometers (from visible to mid-IR) based on different material platforms. The work covering e-SWIR works are highlighted in ***Bold*** for comparison. In terms of spectral resolution, our device demonstrates the best single-peak resolving capability of 17 nm, together with a dual-peak resolving capability of 93 nm. Moreover, our device is the only reported computational spectrometer that operates without an externally applied bias voltage, enabling self-powered operation for energy-efficient spectroscopic systems.

References

1 *InAs photovoltaic detectors*, <https://www.hamamatsu.com/jp/en/product/optical-sensors/infrared-detector/inas-photovoltaic-detector.html> (accessed 11 January 2022.).

2 Li, Z. *et al.* Broadband GaAsSb nanowire array photodetectors for filter-free multispectral imaging. *Nano Letters* **21**, 7388-7395 (2021).

3 LaPierre, R., Robson, M., Azizur-Rahman, K. & Kuyanov, P. A review of III–V nanowire infrared photodetectors and sensors. *Journal of Physics D: Applied Physics* **50**, 123001 (2017).

4 Sun, W. *et al.* High-gain InAs avalanche photodiodes. *IEEE Journal of Quantum Electronics* **49**, 154-161 (2012).

5 Woo, S. *et al.* High-Performance Flexible InAs Thin-Film Photodetector Arrays with Heteroepitaxial Growth Using an Abruptly Graded In x Al1–x As Buffer. *ACS applied materials & interfaces* **13**, 55648-55655 (2021).

6 Zhou, X. *et al.* InAs Photodiodes for 3.43 µm Radiation Thermometry. *IEEE Sensors Journal* **15**, 5555-5560 (2015).

7 Edgar, M. P., Gibson, G. M. & Padgett, M. J. Principles and prospects for single-pixel imaging. *Nature photonics* **13**, 13-20 (2019).

8 Tong, L. *et al.* Stable mid-infrared polarization imaging based on quasi-2D tellurium at room temperature. *Nature communications* **11**, 2308 (2020).

9 Xu, T. *et al.* Van der Waals mid-wavelength infrared detector linear array for room temperature passive imaging. *Science Advances* **10**, eadn0560 (2024).

10 Bullock, J. *et al.* Polarization-resolved black phosphorus/molybdenum disulfide mid-wave infrared photodiodes with high detectivity at room temperature. *Nature Photonics* **12**, 601-607 (2018).

11 Liu, W. *et al.* High-Performance Infrared Self-Powered Photodetector Based on 2D Van der Waals Heterostructures. *Advanced Functional Materials*, 2421525 (2025).

12 Che, M. *et al.* PdSe2/2H–MoTe2 Heterojunction Self-Powered Photodetector: Broadband Photodetection and Linear/Circular Polarization Capability. *ACS nano* **18**, 30884-30895 (2024).

13 Qin, T. *et al.* Mercury telluride colloidal quantum-dot focal plane array with planar pn junctions enabled by in situ electric field–activated doping. *Science Advances* **9**, eadg7827 (2023).

14 Li, Z. *et al.* InAs nanowire arrays for room-temperature ultra-broadband infrared photodetection. *Nanoscale* **15**, 10033-10041 (2023).

15 Park, S. *et al.* Toward Ga-Free Wavelength Extended 2.6 µm InAsP Photodetectors with High Performance. *Advanced Functional Materials* **34**, 2309897 (2024).

16 Ren, D. *et al.* Uncooled Photodetector at Short-Wavelength Infrared Using InAs Nanowire Photoabsorbers on InP with p–n Heterojunctions. *Nano Letters* **18**, 7901-7908 (2018). https://doi.org:10.1021/acs.nanolett.8b03775

17 Yuan, S., Naveh, D., Watanabe, K., Taniguchi, T. & Xia, F. A wavelength-scale black phosphorus spectrometer. *Nature Photonics* **15**, 601-607 (2021).

18 Wang, H., Chen, S. & Chen, X. Room-temperature self-powered infrared spectrometer based on a single black phosphorus heterojunction diode. *Nano Letters* **24**, 326-330 (2023).

19 Deng, W. *et al.* Electrically tunable two-dimensional heterojunctions for miniaturized near-infrared spectrometers. *Nature communications* **13**, 4627 (2022).

20 Yoon, H. H. *et al.* Miniaturized spectrometers with a tunable van der Waals junction. *Science* **378**, 296-299 (2022).

21 Mu, G. *et al.* Hyperspectral quantum-dot image sensors via in-pixel reconfigurable band-alignment. *Nature Photonics*, 1-9 (2026).

22 He, X. *et al.* A microsized optical spectrometer based on an organic photodetector with an electrically tunable spectral response. *Nature Electronics* **7**, 694-704 (2024).

23 Guo, L. *et al.* Balancing Performance and Device Complexity in Single-Point Miniaturized Spectrometers via Multi-Peak Modulation Strategies. *Advanced Materials*, e20521 (2025).

24 Meng, J., Cadusch, J. J. & Crozier, K. B. Detector-only spectrometer based on structurally colored silicon nanowires and a reconstruction algorithm. *Nano Letters* **20**, 320-328 (2019).

25 Cerjan, B. & Halas, N. J. Toward a nanophotonic nose: a compressive sensing-enhanced, optoelectronic mid-infrared spectrometer. *Acs Photonics* **6**, 79-86 (2018).
26 Yu, H. *et al.* A miniaturized cascaded-diode-array spectral imager. *Nature Photonics* **19**, 1322-1329 (2025).
27 Wang, J. *et al.* Single-pixel p-graded-n junction spectrometers. *Nature Communications* **15**, 1773 (2024).